Nanoscale Advances

ROYAL SOCIETY OF CHEMISTRY

PAPER

View Article Online
View Journal

Cite this: DOI: 10.1039/d0na00232a

Vertically aligned nanocomposite $(BaTiO_3)_{0.8}$: $(La_{0.7}Sr_{0.3}MnO_3)_{0.2}$ thin films with anisotropic multifunctionalities†

Xingyao Gao,[a] Di Zhang,[a] Xuejing Wang,[a] Jie Jian,[a] Zihao He,[b] Hongyi Dou[a] and Haiyan Wang *[ab]

Received 25th March 2020
Accepted 11th June 2020

DOI: 10.1039/d0na00232a

rsc.li/nanoscale-advances

A new two-phase $BaTiO_3$: $La_{0.7}Sr_{0.3}MnO_3$ nanocomposite system with a molar ratio of 8 : 2 has been grown on single crystal $SrTiO_3$ (001) substrates using a one-step pulsed laser deposition technique. Vertically aligned nanocomposite thin films with ultra-thin $La_{0.7}Sr_{0.3}MnO_3$ pillars embedded in the $BaTiO_3$ matrix have been obtained and the geometry of the pillars varies with deposition frequency. The room temperature multiferroic properties, including ferromagnetism and ferroelectricity, have been demonstrated. Anisotropic ferromagnetism and dielectric constants have been observed, which can be tuned by deposition frequencies. The tunable anisotropic optical properties originated from the conducting pillars in the dielectric matrix structure, which cause different electron transport paths. In addition, tunable band gaps have been discovered in the nanocomposites. This multiferroic and anisotropic system has shown its great potentials towards multiferroics and non-linear optics.

Introduction

As opposed to the perfect symmetry orders, anisotropic functional oxides, whose electrical, magnetic, or optical properties show directional dependence, have attracted intensive research interest.[1–6] Anisotropic oxides are the ideal candidates for many applications. For example, anisotropic optical thin films can be used in optical devices that operate with polarized light.[7] Among all the anisotropic photonic materials, hyperbolic metamaterials have become an active research topic due to their application in imaging[8–10] and engineering.[11–13] In hyperbolic metamaterials, metals and dielectrics are artificially arranged to form multilayered[14] or nanowire arrays (metal) in the matrix (dielectric)[15] structure. In both structures, the materials show metallic behavior in one direction and dielectric behavior in the other. The big difference between the electric structures of metals and dielectrics is the origin of hyperbolic dispersion and extreme anisotropic optical properties. For instance, in hyperbolic metamaterials, the dielectric constants in different orientations have opposite signs, *i.e.* $\varepsilon_{\parallel} \times \varepsilon_{\perp} < 0$. It has also been proved that hyperbolic dispersion can be observed in the multilayered structure by using a highly doped semiconductor as the metallic layer.[16]

Vertically aligned nanocomposites (VANs) have a unique structure for introducing anisotropy into the thin films. In VANs, two immiscible materials can form a two-phase system with either pillar–pillar or pillar in matrix structures. The use of the vertically aligned pillars can result in a large amount of phase boundaries, which can generate strong strain coupling perpendicular to the film surface. This vertical strain tuning is unique and cannot be observed in layered thin films, which only generate horizontal strain, and can help achieve anisotropic properties that are tunable with the dimension, density or shape of the pillars.[17–19] Metal pillars in oxide matrix VAN structures have been reported and an hyperbolic response has been found in such systems.[20,21]

Inspired by the research on hyperbolic metamaterials, we have designed a VAN system composed of $BaTiO_3$ (BTO) and $La_{0.7}Sr_{0.3}MnO_3$ (LSMO) to achieve anisotropic optical properties. These two materials were selected for the following reasons: first, both BTO and LSMO are commonly studied materials that could be grown on $SrTiO_3$ (STO) substrates (due to the small lattice mismatch with STO) for VAN integration. Second, BTO is a dielectric material while LSMO is a conducting material that can be used as bottom electrodes. By forming a conducting LSMO pillar in the dielectric BTO matrix structure, we expect to see more conducting response in the out-of-plane (OP) direction, which could generate anisotropic optical properties. Third, as BTO and LSMO are reported as room temperature ferroelectric and ferromagnetic materials,[22–25] room temperature multiferroism can be obtained by their combination. A similar approach has been applied for other VAN systems.[26–28] In this work, two deposition frequencies of 2 Hz

[a]School of Materials Engineering, Purdue University, West Lafayette, IN 47907, USA. E-mail: hwang00@purdue.edu

[b]School of Electrical and Computer Engineering, Purdue University, West Lafayette, IN 47907, USA

† Electronic supplementary information (ESI) available. See DOI: 10.1039/d0na00232a

and 10 Hz were utilized for tuning the microstructure of the films, *i.e.* thinner pillars can be obtained by increasing the deposition frequency. The schematic drawing of such designed microstructure change is shown in the top portion of Fig. 1(a). Detailed property measurements have been conducted to demonstrate the anisotropic properties of the BTO : LSMO thin films. The great potential of integrating oxide–oxide VAN thin films with enhanced anisotropic optical properties for optical devices has been proven in this work.

Experimental

The BTO : LSMO target with an 8 : 2 atomic ratio was prepared by a conventional solid-state sintering method. $BaTiO_3$, La_2O_3, $SrCO_3$ and MnO_2 powders were mixed according to the atomic percentage of elements in the composite target. The nanocomposite thin films were deposited onto the STO (001) substrates by the pulsed laser deposition (PLD) technique. During the deposition, the substrates were kept at 750 °C in a 200 mTorr oxygen atmosphere, while a laser with an energy of 420 mJ (laser fluence ~5 J cm^{-2}) was shot onto the targets for 3000 pulses. For all the films, the target to substrate distances were maintained at 4.5 cm. After the deposition, the films were cooled down in a 200 Torr oxygen atmosphere to room temperature at a rate of 10 °C min^{-1}. For the samples that need the electrical property test, a thin layer of $SrRuO_3$ buffer was first deposited onto the substrate as the bottom electrode. The crystallinity of the as-deposited films was checked by X-ray diffraction (XRD, PANalytical Empyrean). Transmittance electron microscopy (TEM, Thermo Scientific TALOS F200X) was utilized for more detailed microstructure examination. The piezoelectric response was investigated using a piezoresponse force microscope (PFM) embedded in an atomic force microscope (AFM, Bruker Dimension Icon). The magnetic response was examined using a magnetic property measurement system (MPMS, Quantum Design MPMS-3). During the measurements, the magnetic fields were applied either parallel (in-plane, or IP as abbreviation) or vertical to the film surface (out-of-plane, or OP as abbreviation). The real dielectric constants were obtained from the ellipsometry results obtained from an RC2 spectroscopic ellipsometer (J.A. Woollam Company). The fitting process was conducted using the Spline or Gen-Osc models in the software from the same company (CompleteEase, J.A. Woollam Company). The transmittance (T%) spectra were obtained using a spectrophotometer (Lambda 1050 UV/Vis spectrophotometer).

Results and discussion

After deposition, the crystallinity of the as-deposited films was investigated by XRD. Fig. 1(b) shows the normalized θ–2θ XRD patterns of the BTO : LSMO thin films deposited at 2 Hz and 10 Hz, respectively. From the XRD patterns, clear BTO (00l) and LSMO (00l) diffraction peaks can be observed, indicating their preferential growth along the OP direction and the separation of the BTO and LSMO peaks demonstrates that these two materials have formed two different phases. Lower intensity of the LSMO peaks might originate from the lower atomic percentage of LSMO (20%) compared with the BTO phase (80%) as well as the size effect where the films have ultra-thin LSMO pillars embedded in the BTO matrix, as demonstrated in the later part. The OP lattice parameters of the BTO and LSMO phases can be calculated using the Bragg's law, which are 4.09 Å for BTO and 4.02 Å for LSMO in the 2 Hz sample. These two values are larger than the OP lattice parameters of their bulk states (4.04 Å for BTO and 3.87 Å for LSMO, marked by the dashed lines in Fig. 1(b)). The same directional change (both increase) of the OP lattice parameters can be explained by the matching BTO, LSMO and STO lattices, as shown in the bottom part of Fig. 1(a). As BTO has a larger IP lattice parameter than STO, compressive strain is generated in the BTO lattices in the IP direction, which enlarges its d-spacing in the OP direction. However, as demonstrated later in the TEM discussion, the LSMO phase has formed vertically aligned pillars with very small diameters,

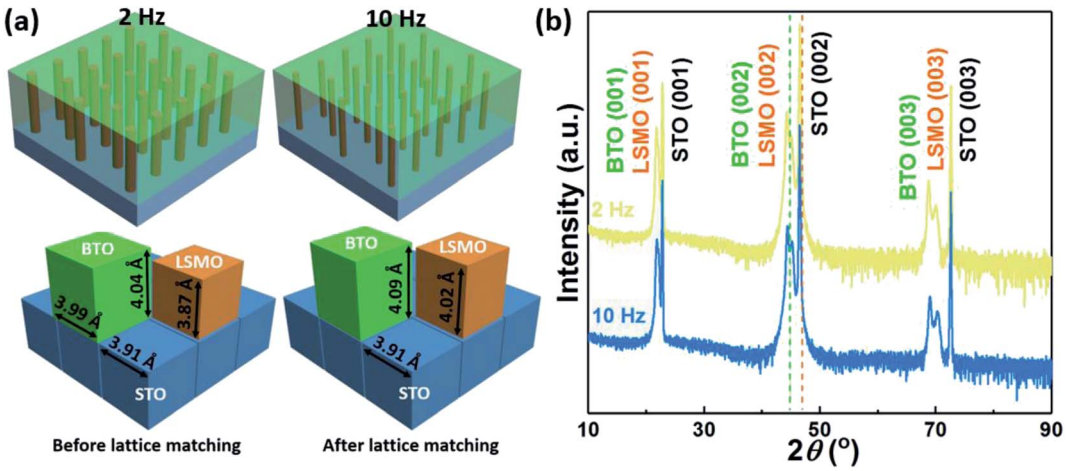

Fig. 1 (a) Designed 3D schematic drawing of the: BTO : LSMO VAN thin films deposited at 2 Hz and 10 Hz (top); lattice parameters of BTO, LSMO and STO before and after the matching (bottom). (b) θ–2θ XRD scans of BTO : LSMO thin films deposited at 2 Hz and 10 Hz. The green and orange dashed lines indicate the (002) peak positions of the bulk BTO and LSMO, respectively.

which significantly decreases the area attached to the substrate and thus limits the strain tuning effect from the substrate. On the contrary, the huge amount of phase boundaries generated by the thin LSMO pillars enhances the tuning effect from the BTO matrix. As a result, the coupling between the BTO and LSMO lattices has become the major tuning factor for LSMO lattices. As the BTO lattice has a larger OP lattice parameter (could be even larger after matching with STO), a tensile strain of 3.87% is generated in the LSMO phase, which elongates the lattice of LSMO along the OP direction to a degree close to that of BTO. No obvious peak shift has been observed as the deposition frequency changes, which might result from the similar pillar dimensions in the films, as demonstrated in the following TEM analysis.

In addition to the XRD scans, TEM was conducted to further understand the microstructure of the BTO : LSMO thin films. The film thicknesses of the 2 Hz and 10 Hz samples were determined to be 90.6 and 117.6 nm, respectively. Fig. 2(a) shows the low-magnification cross-sectional TEM image of the BTO : LSMO thin film deposited at 2 Hz. From the image, it can be observed that the black LSMO pillars are vertically aligned and embedded in the grey BTO matrix, which demonstrates the VAN structure of the BTO : LSMO thin films. The dark cloud-like shadows in the image are possibly generated by the re-deposition of atoms during the TEM sample preparation process. The selected area electron diffraction (SAED) pattern was obtained to demonstrate the orientation relationship of the BTO and LSMO phases as well as the STO substrate, as shown in Fig. 2(b). Only the (00*l*) diffraction dots can be observed along the OP direction, which agrees with the XRD results and indicates the highly textured quality of the BTO : LSMO films. In addition, a matching relationship of $(001)_{BTO}//(001)_{LSMO}//(001)_{STO}$ and $[010]_{BTO}//[010]_{LSMO}//[010]_{STO}$ can be determined from the SAED pattern, which proves the cube on cube growth

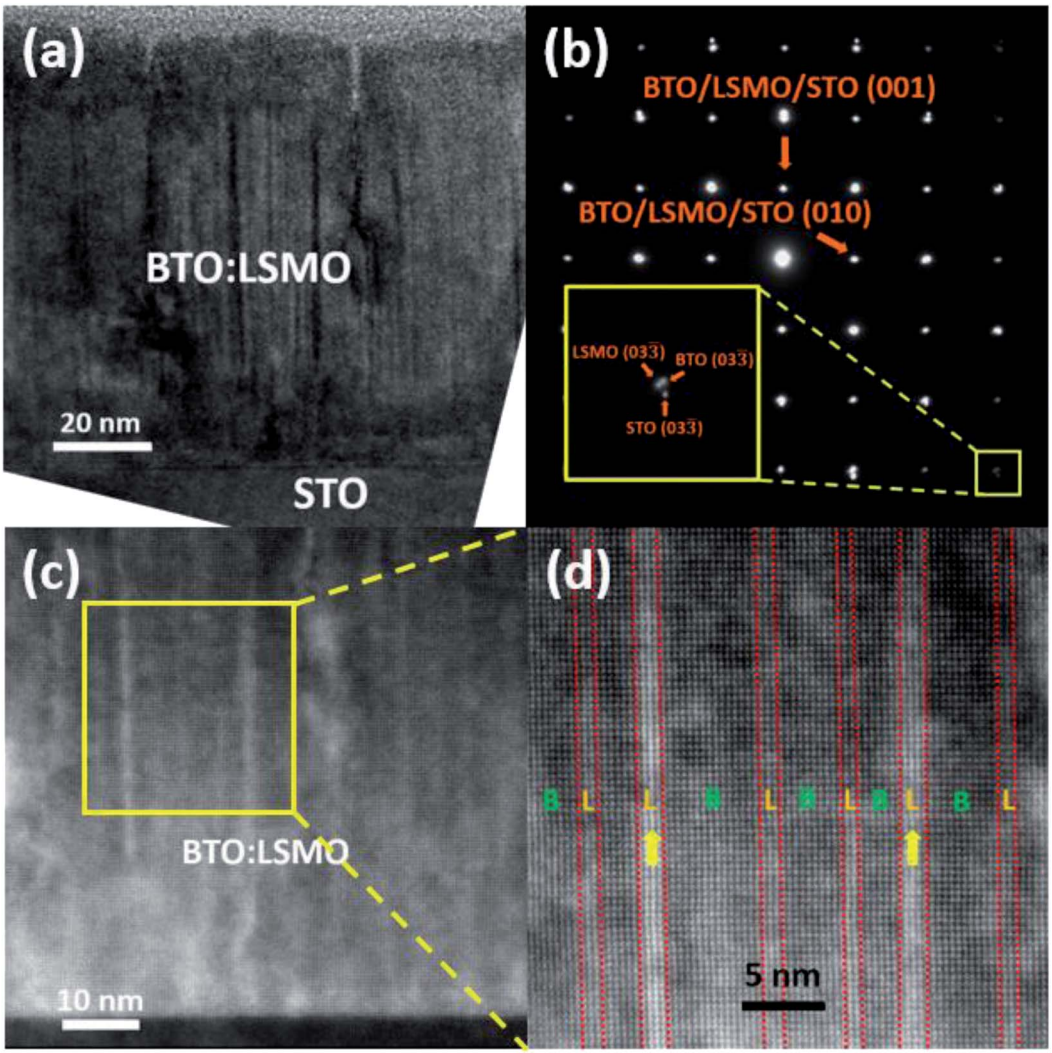

Fig. 2 (a) Cross-sectional TEM image of the 2 Hz BTO : LSMO thin film on STO substrate. (b) SAED pattern of the film and substrate. The inset shows an enlarged image close to the (03$\bar{3}$) dots with clear diffraction dot separation. Cross-sectional (c) STEM and (d) HRSTEM images of the 2 Hz BTO : LSMO nanocomposite. The letters B and L indicate the BTO matrix and LSMO pillars, respectively, while the red dashed lines indicate the phase boundaries.

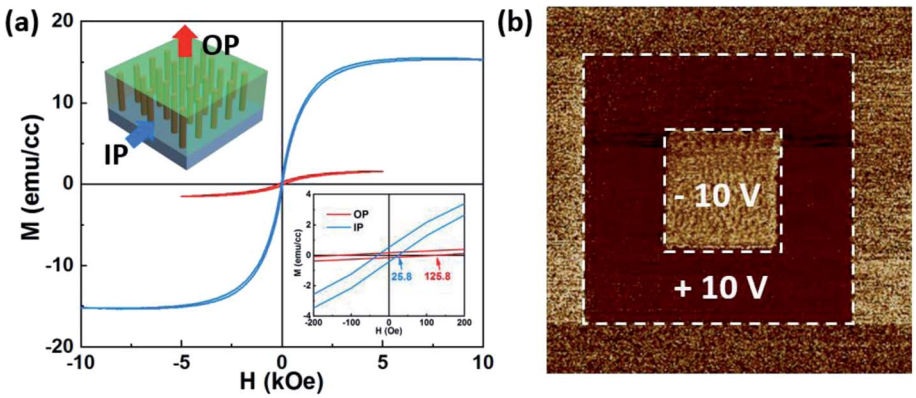

Fig. 3 (a) The room temperature magnetic hysteresis loops of the 2 Hz BTO : LSMO thin film with the magnetic field applied in both IP and OP directions. The top inset demonstrates the direction of the applied magnetic field and the bottom inset shows the enlarged magnetic hysteresis loops close to the original point. (b) The room temperature PFM phase image of the 2 Hz BTO : LSMO thin film with the writing and rewriting tip bias of +10 V and −10 V.

mechanism of the films. The inset in the image shows an enlarged SAED pattern of the $(03\bar{3})$ diffraction dots, where separate dots for BTO, LSMO and STO lattices can be observed, which are merged together when they are close to the original point. Fig. 2(c) shows the scanning transmission electron microscopy (STEM) image of the same sample, where clear LSMO pillars with bright contrast (due to a higher atomic number) are grown perpendicular to the substrate surface. Similar to the TEM image, a re-deposition area can be noticed at the bottom left corner of the image. A high-resolution STEM (HRSTEM) image of the selected area (marked in the yellow square) is shown in Fig. 2(d), where the LSMO pillars and BTO matrix are marked as L and B, respectively. From the HRSTEM image, it can be noted that the LSMO pillars marked with the yellow arrows have ultra-thin diameters of around six unit cells. A large amount of the phase boundary area can be induced by the tiny diameters of the LSMO pillars, which would significantly increase the strain coupling effect between the BTO and LSMO phases along the OP direction. Other pillars without the marks are thinner and lighter than the marked ones, indicating that those pillars are not aligned in the same plane and thus are partially covered by the BTO matrix. Fig. S1† shows the energy-dispersive X-ray spectra (EDS) mapping of the film, where Ti and Mn atoms are marked in yellow and blue, respectively. The EDS mapping confirms the presence of the LSMO pillar in the BTO matrix structure, however, the resolution is relatively low and only a few of the pillars can be observed (marked with red arrows) due to the fine pillar dimension.

The microstructure of the 10 Hz sample was also examined by STEM, as plotted in Fig. S2.† Overall, the film also has the LSMO pillar in the BTO matrix structure with a pillar width of around five unit cells. However, unlike the 2 Hz sample, which has the continuous LSMO pillars from the bottom to the top, some of the pillars inside the 10 Hz sample are discontinuous. This phenomenon can be explained by the diffusion of the adatoms during the deposition, which can be expressed as the following equation: $L \approx 2\sqrt{D\tau}$, where L is the diffusion length of the adatoms, D is the diffusion coefficient and τ is the diffusion time. As the deposition frequency increases from 2 Hz to 10 Hz, the diffusion time (time between the laser pulses) of the adatoms is limited, which generally will cause smaller nucleation islands and decrease the dimension of the pillars grown by those islands, as shown in the top panel of Fig. 1(a).[29,30] However, in this work, as the 2 Hz sample already has ultra-thin pillars that are grown from the tiny nucleation islands, the decreased diffusion time cannot further decrease the dimension of the nucleation islands and the pillar width due to the surface energy. Instead, as the IP diffusion of the adatoms is limited, there is not enough time for the add-on LSMO atoms to move and lie on top of the pre-deposited LSMO atoms to form continuous straight pillars. As a result, some of the LSMO pillars are discontinuous or misaligned, as shown in Fig. S2(b).†

The ferromagnetic response of the BTO : LSMO thin films was measured using a MPMS. Fig. 3(a) shows the ferromagnetic hysteresis loops of a BTO : LSMO film deposited at 2 Hz, with the magnetic field applied parallel and perpendicular to the substrate surface (the magnetic field direction and enlarged hysteresis loops at the original point are illustrated in the inset). It is obvious that the BTO : LSMO nanocomposite shows a room temperature ferromagnetic response, even though this response is relatively weak as a result of the low concentration of LSMO (20%). The coercive fields in both directions are relatively weak, indicating a soft ferromagnetic nature of the film. Besides, the ferromagnetic response also shows IP anisotropy, and a stronger magnetic response in the IP direction than the OP direction can be observed. Similar anisotropic results can be

Table 1 Magnetization of LSMO and BTO : LSMO thin films at 5000 Oe with different measurement orientations

Magnetization at 5000 Oe	LSMO	BTO : LSMO (2 Hz)	BTO : LSMO (10 Hz)
M_{IP}	316.44	15.29	9.52
M_{OP}	7.01	1.54	1.70
M_{IP}/M_{OP}	45.14	9.93	5.60

observed in the 10 Hz and pure LSMO thin films, which are plotted in Fig. S3.† Table 1 summarizes the IP (M_{IP}) and OP (M_{OP}) magnetization of different films at 5000 Oe and their ratio (M_{IP}/M_{OP}) showing the degree of anisotropy. Overall BTO : LSMO films still show IP magnetic anisotropy. When comparing the M_{IP}/M_{OP} values of the BTO : LSMO films with those of the pure LSMO film, it is interesting to note that the anisotropy of the nanocomposites is slowly switched from IP dominating towards OP dominating, suggesting that the shape anisotropy is starting to play a role in the overall magnetic anisotropy. As strain is a key factor influencing the anisotropic ferromagnetism in LSMO thin films,[31–33] the existence of tensile strain in the LSMO pillars could possibly change the easy axis direction from IP to OP and result in this switch. Since some of the pillars are disconnected in the 10 Hz sample, the strain effect from the substrate is further restricted while the vertical strain is more dominating (*i.e.* decreased M_{IP} and increased M_{OP}). The above discussion has demonstrated the tunable room temperature anisotropic ferromagnetic response of BTO : LSMO thin films *via* controlling the deposition frequency (*i.e.* microstructure of pillars).

In addition to the ferromagnetic response, the room temperature ferroelectric properties of the BTO : LSMO thin film were studied. Fig. 3(b) shows the PFM phase image of the 2 Hz sample, while a reversed tip bias of +10 V and −10 V is applied in a square area with the dimensions of $1 \times 1\ \mu m^2$ and $0.5 \times 0.5\ \mu m^2$, respectively. A clear contrast change, indicating the phase change of the thin film, can be noticed as the opposite voltage is applied. In the phase image, the ferroelectric response of the BTO : LSMO thin films is demonstrated, and by coupling with the ferromagnetic hysteresis loops, the overall room temperature multiferroic response is illustrated. This result suggests the potential application of BTO : LSMO thin films in magnetoelectric devices.

The optical properties of the BTO : LSMO thin films were measured using an ellipsometer and the real part of the dielectric constants was fitted from the elliposometry results, as shown in Fig. 4. As shown in Fig. 4(a), anisotropic ellipsometry parameters can be observed in pure BTO films, which have larger IP dielectric constants ($\varepsilon_{\parallel}$) than the OP ones ($\varepsilon_{\perp}$). This phenomenon originated from the substrate induced compressive strain in the BTO lattices, which elongates the lattices in the OP direction and thus allows the electrons to move vertically. As a result, the single phase BTO thin film has anisotropic dielectric constants with lower values in the OP direction. On the other hand, the LSMO thin film shows isotropic dielectric constants, as shown in Fig. 4(b). The isotropic dielectric constants might result from the conducting nature of the LSMO lattices, where the electrons can move equally in both IP and OP directions. Besides, the lower values of the dielectric constants

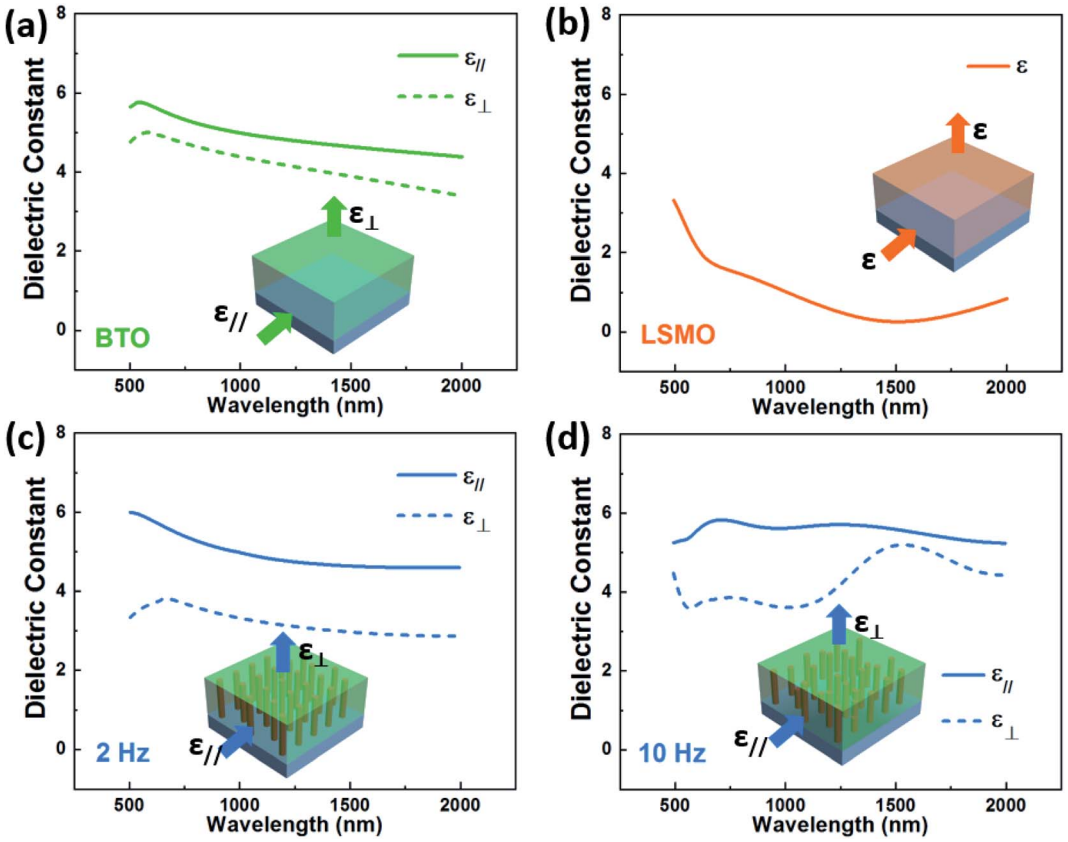

Fig. 4 Fitted real part of the dielectric constants for (a) pure BTO (b) pure LSMO (c) 2 Hz BTO : LSMO and (d) 10 Hz BTO : LSMO thin films. The ordinary and extraordinary curves are plotted in solid and dashed lines, respectively. The fitting direction of the dielectric constants is demonstrated in the inserted schematic drawings.

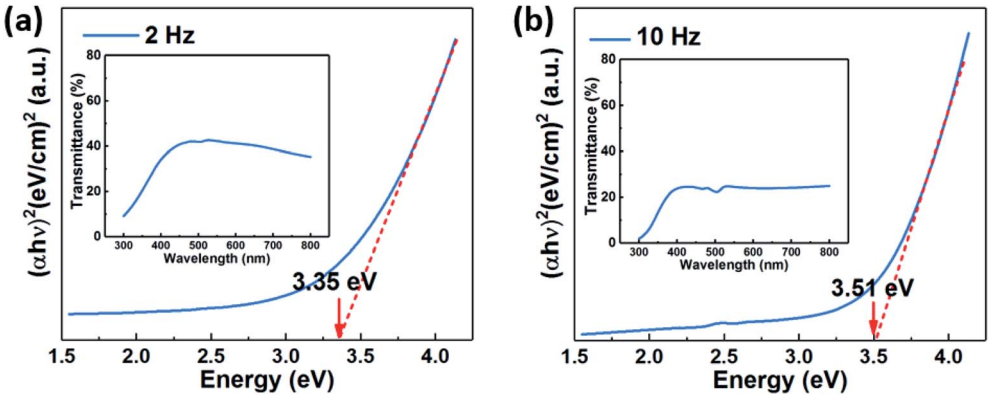

Fig. 5 Direct band gaps of the (a) 2 Hz and (b) 10 Hz BTO : LSMO thin films. The optical band gaps are derived from the transmittance spectra, which are shown as insets.

in LSMO films are predictable due to their high conductivity. The dielectric constants in BTO : LSMO nanocomposites are shown in Fig. 4(c) and (d), where enhanced anisotropy can be observed. In the 2 Hz sample, the vertically aligned LSMO pillars provide easy paths for the electrons to move perpendicularly, which lowers the dielectric constant in the OP direction. On the contrary, since the pillars have tiny diameters, the IP transportation of the electrons is still dominated by the BTO matrix, which results in similar values of the IP dielectric constants compared with the pure BTO film. Enhanced anisotropic dielectric constants can also be found in the 10 Hz sample, even though the properties are not as good as those of the 2 Hz sample due to the discontinuous pillars in the thin film, which limit the transportation of electrons in the OP direction. Overall, the enhanced anisotropic dielectric constants, which are strongly related to the microstructure of the thin films, can be achieved by adding conducting LSMO pillars into the system.

The transmittance of the BTO : LSMO thin films was measured to explore the change of their electronic structures. Fig. 5 shows the band gaps of the BTO : LSMO nanocomposites deposited at 2 Hz and 10 Hz, which are derived from their transmittance spectra (inset in the figures) *via* the Tauc method. The result of the pure BTO film is shown in Fig. S4† as a comparison. It can be noted that the transmittances of the nanocomposites are lower than those of the single phased BTO, which might be caused by the introduction of the secondary phase and the formation of the phase boundaries in the films. Specifically, the 10 Hz sample has lower transmittance than the 2 Hz one as it has a less ordered structure. Besides, the BTO : LSMO thin films have lower band gaps than the pure BTO film which increase as the deposition frequency increases. The decrease of the band gaps in nanocomposites is due to the introduction of the conducting LSMO phase, which has a narrow band gap of 0.63 eV.[34] The LSMO pillars have formed easy paths for the electron transportation, which subsequently decreases the band gap of the films. From the TEM analysis, these "paths" are more continuously aligned in the 2 Hz sample, and thus a lower band gap can be found in the sample with a deposition frequency of 2 Hz.

In this work, the design of embedding conducting oxide pillars into the dielectric oxide matrix presents an approach for obtaining tunable anisotropic optical properties. The VAN structure can provide multiple tuning parameters, including the oxygen pressure, substrate temperature, deposition frequency and energy for the microstructure and strain tuning. By the material selections, tunable anisotropic multifunctionalities, including ferroelectricity, ferromagnetism and optical properties can be obtained in VAN thin films.

Conclusion

In summary, we have reported a VAN system with the composition of $(BaTiO_3)_{0.8}$: $(La_{0.7}Sr_{0.3}MnO_3)_{0.2}$, which is grown onto STO (001) substrate *via* PLD. The cross-sectional TEM and STEM images have demonstrated that the ultra-thin LSMO pillars with a dimension of around five unit cells were embedded in the BTO matrix. By changing the deposition frequencies from 2 Hz to 10 Hz, the arrangement of the pillars are tuned from continuous to partially discontinuous alignment. With the pillar geometry change, the anisotropy of the ferromagnetic properties has been tuned from IP dominating towards OP dominating, which might be attributed to the change of the easy magnetization axis rotation in the LSMO lattices. Accompanied by the ferroelectric response, the room temperature multiferroic properties have been obtained. The vertically aligned conducting pillars have provided an easy transport path for the electrons, and thus the anisotropic dielectric constants in the nanocomposite have been enhanced compared to those of the pure BTO film. In addition to the dielectric constants, tunable band gaps have also been achieved in this system. The BTO : LSMO system presents enormous application opportunities in data storage devices and non-linear optical devices.

Conflicts of interest

There are no conflicts to declare.

Acknowledgements

This work was supported by the U.S. National Science Foundation (DMR-1565822). D. Z. and J. J. acknowledge the partial support from the U.S. Office of Naval Research (N00014-20-1-2043) for optical measurements. Z. H. acknowledges the support from the U.S. National Science Foundation (DMR-1809520). H. D. acknowledges the support from the U.S. National Science Foundation (ECCS-1902644).

References

1 D. Lisjak and A. Mertelj, Anisotropic Magnetic Nanoparticles: A Review of Their Properties, Syntheses and Potential Applications, *Prog. Mater. Sci.*, 2018, **95**, 286–328.

2 C. Daboo, R. J. Hicken, R. Gu, M. Gester, S. J. Gray, D. E. P. Eley, E. Ahmad and J. A. C. Bland, Anisotropy and Orientational Dependence of Magnetization Reversal Processes in Epitaxial Ferromagnetic Thin Films, *Phys. Rev. B: Condens. Matter Mater. Phys.*, 1995, **51**, 15964–15973.

3 H. N. Lee and D. Hesse, Anisotropic Ferroelectric Properties of Epitaxially Twinned $Bi_{3.25}La_{0.75}Ti_3O_{12}$ Thin Films Grown with Three Different Orientations, *Appl. Phys. Lett.*, 2002, **80**, 1040–1042.

4 M. D. Tocci, M. J. Bloemer, M. Scalora, J. P. Dowling and C. M. Bowden, Thin-Film Nonlinear Optical Diode, *Appl. Phys. Lett.*, 1995, **66**, 2324–2326.

5 S. Misra, L. Li, X. Gao, J. Jian, Z. Qi, D. Zemlyanov and H. Wang, Tunable Physical Properties in $BiAl_{1-x}MnxO_3$ Thin Films with Novel Layered Supercell Structures, *Nanoscale Adv.*, 2020, **2**, 315–322.

6 X. Gao, L. Li, D. Zhang, X. Wang, J. Jian, Z. He and H. Wang, Novel Layered $Bi_3MoM_TO_9$ (M_T = Mn, Fe, Co and Ni) Thin Films with Tunable Multifunctionalities, *Nanoscale*, 2020, **12**(10), 5914–5921.

7 H. Seiberle, C. Benecke and T. Bachels, Photo-Aligned Anisotropic Optical Thin Films, *J. Soc. Inf. Disp.*, 2004, **12**, 87–92.

8 Z. Liu, H. Lee, Y. Xiong, C. Sun and X. Zhang, Far-Field Optical Hyperlens Magnifying Sub-Diffraction-Limited Objects, *Science*, 2007, **315**, 1686.

9 J. Rho, Z. Ye, Y. Xiong, X. Yin, Z. Liu and H. Choi, Spherical Hyperlens for Two-Dimensional Sub-Diffractional Imaging at Visible Frequencies, *Nat. Commun.*, 2010, **1**, 143.

10 Z. Jacob, L. V. Alekseyev and E. Narimanov, Optical Hyperlens: Far-Field Imaging beyond the Diffraction Limit, *Opt. Express*, 2006, **14**, 8247–8256.

11 Y. Guo, C. L. Cortes, S. Molesky and Z. Jacob, Broadband Super-Planckian Thermal Emission from Hyperbolic Metamaterials, *Appl. Phys. Lett.*, 2012, **101**, 131106.

12 X. Yang, J. Yao, J. Rho, X. Yin and X. Zhang, Experimental Realization of Three-Dimensional Indefinite Cavities at the Nanoscale with Anomalous Scaling Laws, *Nat. Photonics*, 2012, **6**, 450–454.

13 A. Poddubny, I. Iorsh, P. Belov and Y. Kivshar, Hyperbolic Metamaterials, *Nat. Photonics*, 2013, **7**, 958–967.

14 Z. Jacob, J.-Y. Kim, G. V. Naik, A. Boltasseva, E. E. Narimanov and V. M. Shalaev, Engineering Photonic Density of States Using Metamaterials, *Appl. Phys. B*, 2010, **100**, 215–218.

15 J. Gao, X. Wu, Q. Li, S. Du, F. Huang, L. Liang, H. Zhang, F. Zhuge, H. Cao and Y. Song, Template-Free Growth of Well-Ordered Silver Nano Forest/Ceramic Metamaterial Films with Tunable Optical Responses, *Adv. Mater.*, 2017, **29**, 1605324.

16 P. Shekhar and Z. Jacob, Strong Coupling in Hyperbolic Metamaterials, *Phys. Rev. B: Condens. Matter Mater. Phys.*, 2014, **90**, 045313.

17 X. Gao, L. Li, J. Jian, J. Huang, X. Sun, D. Zhang and H. Wang, Tunable Low-Field Magnetoresistance Properties in $(La_{0.3}Ca_{0.3}MnO_3)_{1-x} : (CeO_2)_x$ Nanocomposite Thin Films, *Appl. Phys. Lett.*, 2019, **115**, 053103.

18 Q. Su, W. Zhang, P. Lu, S. Fang, F. Khatkhatay, J. Jian, L. Li, F. Chen, X. Zhang, J. L. MacManus-Driscoll, *et al.*, Self-Assembled Magnetic Metallic Nanopillars in Ceramic Matrix with Anisotropic Magnetic and Electrical Transport Properties, *ACS Appl. Mater. Interfaces*, 2016, **8**, 20283–20291.

19 W. Zhang, A. Chen, Z. Bi, Q. Jia, J. L. Macmanus-driscoll and H. Wang, Interfacial Coupling in Heteroepitaxial Vertically Aligned Nanocomposite Thin Films: From Lateral to Vertical Control, *Curr. Opin. Solid State Mater. Sci.*, 2014, **18**, 6–18.

20 S. Misra, L. Li, D. Zhang, J. Jian, Z. Qi, M. Fan, H. Chen, X. Zhang and H. Wang, Self-Assembled Ordered Three-Phase Au–$BaTiO_3$–ZnO Vertically Aligned Nanocomposites Achieved by a Templating Method, *Adv. Mater.*, 2019, **31**, 1806529.

21 J. Huang, X. Wang, X. L. Phuah, P. Lu, Z. Qi and H. Wang, Plasmonic Cu Nanostructures in ZnO as Hyperbolic Metamaterial Thin Films, *Materials Today Nano*, 2019, **8**, 100052.

22 K. J. Choi, M. Biegalski, Y. L. Li, A. Sharan and J. Schubert, Enhancement of Ferroelectricity in Strained $BaTiO_3$ Thin Films, *Science*, 2004, **306**, 1005–1010.

23 K. Steenbeck, T. Habisreuther, C. Dubourdieu and J. P. Senateur, Magnetic Anisotropy of Ferromagnetic $La_{0.7}Ca_{0.3}MnO_3$ Epitaxial Thin Films: Dependence on Temperature and Film Thickness, *Appl. Phys. Lett.*, 2002, **80**, 3361–3363.

24 D. Kan and Y. Shimakawa, Controlled Cation Stoichiometry in Pulsed Laser Deposition-Grown $BaTiO_3$ Epitaxial Thin Films with Laser Fluence, *Appl. Phys. Lett.*, 2011, **99**, 081907.

25 A. P. Chen, F. Khatkhatay, W. Zhang, C. Jacob, L. Jiao and H. Wang, Strong Oxygen Pressure Dependence of Ferroelectricity in $BaTiO_3/SrRuO_3/SrTiO_3$ Epitaxial Heterostructures, *J. Appl. Phys.*, 2013, **114**, 124101.

26 X. Gao, L. Li, J. Jian, H. Wang, M. Fan, J. Huang, X. Wang and H. Wang, Vertically Aligned Nanocomposite $BaTiO_3 : YMnO_3$ Thin Films with Room Temperature Multiferroic Properties toward Nanoscale Memory Devices, *ACS Appl. Nano Mater.*, 2018, **1**, 2509–2514.

27 H. Wang, L. Li, J. Huang, X. Gao, X. Sun, D. Zemlyanov and H. Wang, Two-Phase Room-Temperature Multiferroic Nanocomposite with $BiMnO_3$-Tilted Nanopillars in the

$Bi_2W_{1-x}Mn_xO_6$ Matrix, *ACS Appl. Mater. Interfaces*, 2019, **11**, 26261–26267.

28 H. Wang, L. Li, J. Huang, X. Gao, X. Sun and H. Wang, Multiferroic Vertically Aligned Nanocomposite with $CoFe_2O_4$ Nanocones Embedded in Layered Bi_2WO_6 Matrix, *Mater. Res. Lett.*, 2019, **7**, 418–425.

29 A. Chen, Z. Bi, Q. Jia, J. L. Macmanus-driscoll and H. Wang, Microstructure , Vertical Strain Control and Tunable Functionalities in Self-Assembled, Vertically Aligned Nanocomposite Thin Films, *Acta Mater.*, 2013, **61**, 2783–2792.

30 Z. Bi, J. H. Lee, H. Yang, Q. Jia, J. L. MacManus-Driscoll and H. Wang, Tunable Lattice Strain in Vertically Aligned Nanocomposite $(BiFeO_3)_x : (Sm_2O_3)_{1-x}$ Thin Films, *J. Appl. Phys.*, 2009, **106**, 094309.

31 F. Tsui, M. C. Smoak, T. K. Nath and C. B. Eom, Strain-Dependent Magnetic Phase Diagram of Epitaxial $La_{0.67}Sr_{0.33}MnO_3$ Thin Films, *Appl. Phys. Lett.*, 2000, **76**, 2421–2423.

32 Y. Suzuki, H. Y. Hwang, S.-W. Cheong and R. B. van Dover, The Role of Strain in Magnetic Anisotropy of Manganite Thin Films, *Appl. Phys. Lett.*, 1997, **71**, 140–142.

33 A. Chen, J. M. Hu, P. Lu, T. Yang, W. Zhang, L. Li, T. Ahmed, E. Enriquez, M. Weigand, Q. Su, *et al.*, Role of Scaffold Network in Controlling Strain and Functionalities of Nanocomposite Films, *Sci. Adv.*, 2016, **2**, 1600245.

34 H. Lee and H. Park, Band Structure Analysis of $La_{0.7}Sr_{0.3}MnO_3$ Perovskite Manganite Using a Synchrotron, *Adv. Condens. Matter Phys.*, 2015, **2015**, 746475.

